Structure-dynamics correlations in composite PF127-PEG-based hydrogels; cohesive/hydrophobic interactions determine phase and rheology and identify the role of micelle concentration in controlling 3D extrusion printability

Krutika Singh[1], Jacek K. Wychowaniec[1,2,*], Charlotte J.C. Edwards-Gayle[3], Emmanuel G. Reynaud[4], Brian J. Rodriguez[4,5], Dermot F. Brougham[1,*]

[1] School of Chemistry, University College Dublin, Belfield, Dublin 4, Ireland

[2] AO Research Institute Davos, Clavadelerstrasse 8, 7270, Davos, Switzerland

[3] Diamond Light Source, Harwell Science and Innovation Campus, Fermi Avenue, Didcot, OX110DE

[4] Conway Institute of Biomolecular and Biomedical Research, University College Dublin, Belfield, Dublin 4, Ireland

[5] School of Physics, University College Dublin, Belfield, Dublin 4, Ireland

* Corresponding authors:

J.K.W. Phone: (+41)0779238956;

e-mail: jacek.wychowaniec@aofoundation.org

D.F.B. Phone: (+353)017162077;

e-mail: dermot.brougham@ucd.ie

Graphical Abstract

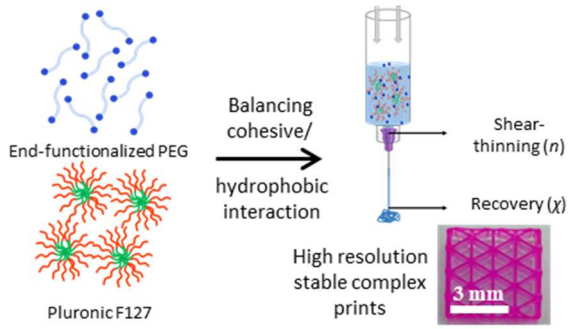

Abstract

A library of composite polymer networks (CPNs) were formed by combining Pluronic F127, as the primary gelator, with a range of di-acrylate functionalised PEG polymers, which tune the rheological properties and provide UV crosslinkability. A coarse-grained sol-gel room temperature phase diagram was constructed for the CPN library, which identifies PEG-dependent disruption of micelles as leading to liquefication. Small angle X-ray scattering and rheological measurements provide detailed insight into; (i) micelle-micelle ordering; (ii) micelle-micelle disruption, and; (iii) acrylate-micelle disruption; with contributions that depend on composition, including weak PEG chain length and end group effects. The influence of composition on 3D extrusion printability through modulation of the cohesive/hydrophobic interactions was assessed. It was found that only micelle content provides consistent changes in printing fidelity, controlled largely by printing conditions (pressure and feed rate). Finally, the hydrogels were shown to be UV photo-crosslinkable, which further improves fidelity and structural integrity, and usefully reduces the mesh size. Our results provide a guide for design of 3D-printable CPN inks for future biomedical applications.

Keywords: Composite polymer networks; structure-dynamics relationships; polyethylene(glycol); Pluronic F127 (PF127); 3D extrusion-based printing.

Introduction

Fabricating complex bio-mimetic cell supports for tissue engineering (TE), that recapitulate the native environment, requires development of bio-compatible matrices that have good rheological properties (for fabrication/structuring),[1-3] tuneable stiffness (to influence cell fate/lineage),[4, 5] and which can be solidified (and so remain intact for extended periods in complex aqueous environments)[6] while having controlled degradation profiles [6-9]. Hydrogels are commonly studied as they can meet these criteria, and because of their similarities to the extracellular matrix, water retention capabilities and potential for chemical modification and compositing.[10-13] For advanced extrusion-based manufacturing of cell supports printability and good print quality are also required, so the hydrogels should be shear-thinning (reduced viscosity at increased shear) with rapid recovery to the original state.[3, 14] These factors are determined by polymer M_n, concentration and charge, and by the extent of entanglement and network topology which are influenced by inter-molecular interactions.[15-19] For composite polymer networks (CPNs) these interaction can in principle be tuned through composition.

Pluronic F127, also known as PF127 or Poloxomer 407, is a polymer widely used in hydrogel formulation. PF127 is a block-co-polymer composed of poly(ethylene) oxide (PEO) and more hydrophobic polypropylene oxide (PPO) which renders it thermoresponsive,[20, 21] ***Figure 1A***, it has M_n *c.*12.6 kDa and the average formula PEO_{100}–PPO_{65}–PEO_{100}. In the higher concentration range micelles form with the PPO blocks oriented towards each other providing a hydrophobic core and the PEO units oriented outwards, ***Figure 1A***. At temperatures above the sol to gel phase transition self-assembly of the micelles occurs.[22] PF127 is shear thinning [14, 23] and easy to handle, so it is commonly used to modify the rheological properties of other materials,[24, 25] and fillers are used to modify the rheological properties of Pluronic.[26] So, for instance, PF127 has been commonly exploited as a fugitive ink for 3D

printing of complex structures.[27-30] It has also been used as the main matrix former [31, 32] and as a component in CPN hydrogels, *e.g.* for maintaining cell proliferation and differentiation.[33-35] PF127 is soft, with rheological properties suitable for high quality 3D (bio)printing. However, it must be cross-linked to retain stability in media and fidelity of the fabricated structures.

Many approaches to improve the physicochemical properties of PF127 and to impart better biological characteristics have been reported, and this field has been recently reviewed. [36] These include chemical modification of the PF127 backbone,[37, 38] and inclusion of other hydrophilic polymers as secondary networks,[24, 39-42] the latter is more relevant to our study. For instance, simple physical mixing of PF127, at ~20% w/v, with hyaluronic acid (M_w ~1000 kDa), at ~1% w/v, has been described. The resulting 'physical' hydrogel had its phase transition *c.*31 °C, which is similar to PF127, but with 1.4-times higher viscous modulus. Apparently, HA increases both the packing density and interactions between micelles increasing stiffness and the gels mechanical stability. Physical composite hydrogels were also prepared by mixing P407 with chitosan (20 and 20% w/v, respectively) with prolonged dexamethasone release demonstrated, as compared to pure P407.[40] Modelling suggested that crosslinking reduced chain relaxation (altering the release profile) for the composite, as compared to rapid micelle disentanglement for the single component hydrogel. In a recent study Kushan and Senses investigated a panel of hydrogels composed of cellulose nanocrystals (CNCs) and PF127.[42] They reported that at low CNC loading (1-3 wt%) hydrophobic interactions between CNC and the PPO block dominated, resulting in the disruption of micelle-micelle interactions, softening the nanocomposite gels. At higher loading, of 4-5 wt%, a secondary network formed entrapping micelles and increasing toughness.

Poly(ethylene glycol) diacrylate [7-9, 16, 43-45] is widely used as an additive for network formation in CPN formulations providing hydration, UV photo-crosslinkability.[46-

48] Cellular viability has been demonstrated for hydrogels formed using bi-functional PEG with different functional groups. These also provide possibilities for tuning the degradability; diacrylates offer fast degradation, while for diacrylamides degradation over up to a month in vitro and in vivo has been reported.[7-9, 43, 45, 49] PEG-based networks can also be functionalised, *e.g.* with peptides, to increase cell adhesion and promote cellular proliferation and eventual remodelling.[7, 44] Pure PEGDA formulations cannot be used for extrusion as they lose shape on deposition and require secondary polymer stabilisation.[47]

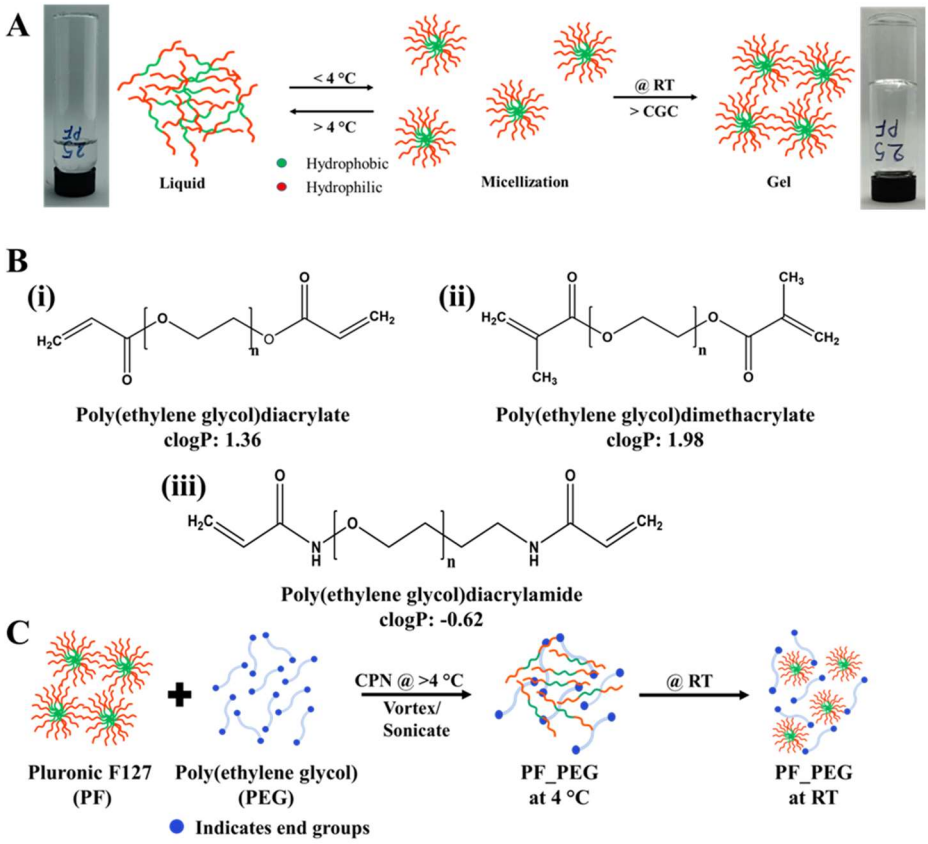

Figure 1: ***(A)*** *Schematic depiction of the thermoreversible phase transition of PF127;* ***(B)*** *Chemical structures of functionalised PEG-based polymers: (i) Poly(ethylene glycol)diacrylate (clogP 1.36); (ii) Poly(ethylene glycol) dimethacrylate (clogP 1.98); (iii) Poly(ethylene glycol) diacrylamide (clogP -0.62); clogP values are calculated for n=1 in all cases, the approach is described in Methods.* ***(C)*** *Representation of the temperature induced*

self-assembly of composite polymer network (CPN) hydrogels using PF127 (shown as micelles, with green part displaying hydrophobic PPO block and red parts displaying hydrophilic PEO blocks) and functionalised-PEG (in blue).

Given the demonstrated potential for modulating nanocomposite gel properties, and the drawbacks of pure PF127 and pure PEG for TE applications; in this study a library of inks was fabricated, using PF127 and a range of bi-functional PEGs, ***Figure 1A-B***, with a view to combining the advantageous properties of each component to meet the broad requirements of TE. The goals were; (i) to assess the structure-dynamics relationships to gain insight into how structural ordering affects rheology, and; (ii) from a practical perspective to exploit the thermosensitivity and printability of PF127, while compensating for its intrinsic softness with the PEG component which also provides crosslinkability. Using facile temperature-induced self-assembly, ***Figure 1C***, the influence of the composition of each component on gelation, internal structure and rheological properties was assessed. Composition-dependent disruptive interactions were identified. These outcomes were then correlated, in so far as proves possible, with the quality of printed structures evaluated as a function of printing parameters.

Materials and Methods

Chemicals: Pluronic® F-127 (PF), poly(ethyleneglycol) diacrylate (PEGDA, M_n 700, 2000 & 20000), polyethylene glycol (PEG, M_n 2000), poly(ethylene glycol) dimethacrylate (PEGDMA M_n 750) and poly(ethylene glycol) diacrylamide (PEGDAA M_n 3700), 2-hydroxy-2-methylpropiophenone (HMPP, 97%) were purchased from Sigma Aldrich (Merck Co.) and used as-received. Type 1 ultrapure water (H_2O) of 18.2 MΩ resistance (from Purelab® Flex system) was used in all experiments.

PF127-Functionalised polyethylene glycol composite polymer network (CPN) inks preparation: Different concentrations of gels with 10 – 30 w/v% (all compositions are in w/v% which will be shortened to %) or just of functionalised-PEG, or PEG with OH end groups, 25 – 45% of PF127 and 1% HMPP were all mixed to form a gel as shown in ***Figure 1A*** in H_2O. The samples are labelled as xPF_yPEGzMW, where x defines concentration of PF (Pluronic F127) in w/v%, y defines concentration of functionalised PEG in w/v%, z defines the functional group (DA, DMA, DAA, or none indicating OH end groups on PEG) and MW defines the PEG molecular weight. The x and/or y labels are omitted when indicating a series of formulations, *e.g.* x25PF_10PEGDA700.

The process followed to prepare 5 mL of the 25PF_10PEGDA700_1HMPP formulation, for example, is as follows; in a clean glass vial 0.5 g of PEGDA700 was weighed out to which 0.046 mL (46 µL) HMPP and 1 mL H_2O was added. The sample was vortexed for 1 min to mix the solutions. 1.25 g of PF127 was then added with the remaining of 3.504 mL of H_2O. The formulation was then vortexed and immediately stored at 4 ºC. After 30 mins the formulation was vortexed and placed back at 4 ºC. This process was repeated at least 3 times and the vial was inspected each time for visually undissolved PF127 lumps. Any persistently inhomogeneous samples were discarded. The homogeneous formulations were then left undisturbed for another 4-14 hrs, depending on the type of formulation. Once a clear solution was obtained the formulations were removed from 4 ºC and stored at RT until use. All quantities used to make 5 mL of each formulation is shown in ***Table S1***.

clogP values were estimated for the structures drawn in ***Figure 1B*** using ChemDraw Professional 16.0. The calculations were done by drawing structures with different number of monomer units in the chain (n) from 1 to 3 to evaluate any effect of the polymer backbone on the calculated values, ***Table S2***. Encouragingly the end group type had the strongest influence on the *clogP* values, and the values are very different for the three end-group types. On the

other hand the values did not vary much with n, but rather started to oscillate slightly. Hence, we include *clogP* values for n=1 in ***Figure 1B***, as representative of each end-group.

Gelation Phase Diagrams: Samples were prepared directly, as described above, and initially stored in a fridge (4 °C) for 24 h, followed by 20 mins storage at 22 °C before their physical state was examined. Samples were classified as liquid if they flowed freely upon inversion of vials, and as gels if they did not freely flow.

Small angle x-ray scattering (SAXS): Small Angle X-ray Scattering was performed at B21, Diamond Light Source, UK.[50] Samples were loaded into either PEI capillaries or MPS sticks enclosed with Kapton tape and loaded into the MPS sample cell.[51] Details of experimental set up and modelling can be found in the Supporting Information and in the provided references.[50, 51]

Rheological Evaluation: The rheology was performed on MCR301 rheometer from Anton Paar. Parallel plate geometry with a 25 mm diameter top plate and, unless otherwise stated, 0.5 mm gap was used. About 200 μL of sample was placed on the bottom plate using a spatula, and subsequently the top rheometer plate was lowered slowly to minimise hydrogel disruption for each measurement. Viscosity versus temperature tests were performed in a rotational mode at a shear rate of 0.1 s^{-1} within room temperature range from 20 to 30 ºC, at a 0.5 ºC min^{-1} heating rate. Prior to temperature experiments, all samples were equilibrated for 2 mins. To avoid sample evaporation the humidity control hood was used. All viscosity-shear rate experiments (flow curves) were performed at 22 °C, with samples subjected to shear rate from 0.01 to 2000 s^{-1}, and being held at each shear rate until a stable reading was reported by the instrument. The shear thinning behaviour was characterised by fitting the Power Law equation (1) to the linear region of the shear rate-viscosity rheology plot.

$$\eta = K\dot{\gamma}^{n-1} \qquad (1)$$

where η is the viscosity, $\dot{\gamma}$ the shear rate, K a consistency value and n the shear thinning exponent.

Recovery tests were performed in a rotational mode by initially subjecting sample to shear close to a zero-shear value (0.01 s^{-1}) for 200 seconds. Then shear rate was increased to 895 s^{-1} and kept for 100 seconds. Recovery was then monitored for 200 seconds by switching the shear rate back to 0.01 s^{-1}. All recovery tests were performed at 22 °C. All measurements were repeated at least two times, and average and standard deviation presented. Percentage recovery was calculated using the values obtained from recovery test in the following way:

$$\chi = \frac{\eta_{@\,340\,s}}{\eta_{@\,200s}} \times 100 \qquad (2)$$

where χ denotes % recoverability, $\eta_{@\,340\,s}$ is the equilibrated viscosity value after the increased shear rate (3rd interval) and $\eta_{@\,200\,s}$ is the last viscosity value of the 1st interval, before increased shear rate was applied. The error for those values was estimated from two recoverability values from independent experiments.

To establish the effect of UV crosslinking (described below), frequency sweeps were performed in oscillatory mode from 0.1 to 15 Hz at 0.2% strain within the linear viscoelastic regime of all the samples at 22 °C. Briefly 800 µL of hydrogel was added to a 12 well-plate (with diameter, $d \approx 25$ mm) and UV-crosslinked with cover off, as described below. Hydrogels were then carefully removed from the well-plate and directly placed on the bottom rheometer plate. The top rheometer plate was lowered slowly to minimise hydrogel disruption for each measurement. Prior to frequency tests, all hydrogels were equilibrated for 3 mins.

UV-crosslinking: All the PF_PEG samples shown in ***Figure 2*** that formed hydrogels were tested for crosslinkability. The UV setup was prepared as follows; briefly 800 µL of hydrogel was added to a 12 well-plate and irradiated using an in-house set-up consisting of 8 LEDs (Mfr. No: LZ1-30UV00-0000, Mouser Electronics, UK), arranged into a 3D-printed ring with peak wavelength at λ=365 nm and total irradiation power of 16 mW cm^2 (***Figure S1***) for time

ranging from 30 seconds to 10 minutes. To determine crosslinking time, a spatula test was performed to estimate UV exposure time for full crosslinking, which was subsequently confirmed by oscillatory rheology. The results of this study, including the observations and tested times for each formulation are described in supporting information in ***Table S3***.

3D printing: Printability of hydrogels was evaluated using a dual-head Allevi-2 bioprinter. Samples were removed from the refrigerator and immediately transferred as liquids (at *c.*4°C) into the syringe and immediately returned to refrigerator for 10 mins to remove any potential bubbles. Then, prior to printing, syringes were finally rested at 22 °C for 30 mins. Each gel was printed into a 15 x 15 mm grid, using a straight stainless-steel needle with 152 μm inner diameter. Different head velocities 400 – 1000 mm min^{-1} and pressure 2.89 – 3.44 bar were used for different formulations (for details see main text). The parameters used are summarised in ***Table 1***. The prints were imaged using 2X magnification on an Olympus BX51 Microscope, in most cases, 30-45 seconds after printing has finished (related to moving samples between laboratories). Finally, captured images were analysed using ImageJ to establish thickness of lines within printed grids, based on at least 9 vertical (Y) and at least 8 horizontal (X) measurements, represented as averages ± standard deviation. G-codes used for printing the grids are provided as supporting .txt files, see SI.

Table 1. *Parameters used for printing.*

Parameter	Symbol	Value
Functionalised PEGs	PEG	10 – 30 w/v%
Pluronic F127	PF127	25 – 45 w/v%
Head temperature	T	22 °C
Needle length	L	12.7 mm
Needle inner diameter	D	0.15 mm
Extrusion pressure	f	2.89 – 3.44 bar
Head velocity	ν	400 – 1000 mm min^{-1}

Results and Discussion

This section is organised as follows; (i) CPNs formation and analysis of the influence of PEG-Pluronic interactions on the phase behaviour; (ii) SAXS analysis of CPNs, placing the phase diagram on a stronger physical basis; (iii) temperature dependent gelation and rheology of CPNs, relating dynamics to structure; (iv) assessment of links between rheology and printability, and; (v) 3D printing and photo-crosslinking of the final CPN formulations.

(i) Formation of composite polymer network hydrogels; binary phase diagram

First, we examined the effect of compositing with PEG on micellisation/hydrogelation of PF127. CPN ink formulations were prepared using PF127 with three different acrylate-functionalised PEGs as additives, ***Figure 1B-C***; diacrylate (DA); dimethacrylate (DMA); diacrylamide (DAA), and also PEG with OH end groups as a control. The formulations are labelled as, *e.g.* 25PF_yPEGDA700 for the series with 25% PF127 and variable (y) PEG diacrylate (M_n 700) content, or 30PF_20PEGDMA750 for the single formulation with 30% PF127 and 20% PEGDMA (M_n 750). All formulations included 1% HMPP photo-initiator for photo-curing after printing.

Hydrogel formation was assessed initially using inverted vial tests for samples of different PF127 and PEG content and PEG molecular weight, ***Figures S2*** and ***S3***. The latter is known to affect gelation and network mesh size.[52] For PF127 the phase transition temperature depends on polymer concentration and the presence and concentration of salts or additives which can disrupt micellisation.[21, 53, 54] The critical gelation concentration (CGC) values quoted in the literature range from 15-25 w/v%.[54-56] Our preliminary tests showed gelation for PF127 at 22 °C in pure water at >21%. Compositions from 25% Pluronic (given the pure PF127 CGC of ~21%) and from 10% PEGDA (the lowest reported composition for TE [8]) were measured to reveal a coarse-grained phase diagram for the different series at 22

°C, ***Figure 2***. The presence of PEG polymers disrupted hydrogelation; for all PEG types (except PEGDA20K, see below) there was at least one PF127 content identified at which the CPN was a liquid, while all the pure PF127 samples were gels. The following detailed analysis shows that disruption of gelation is dependent on both chain length and end group type.

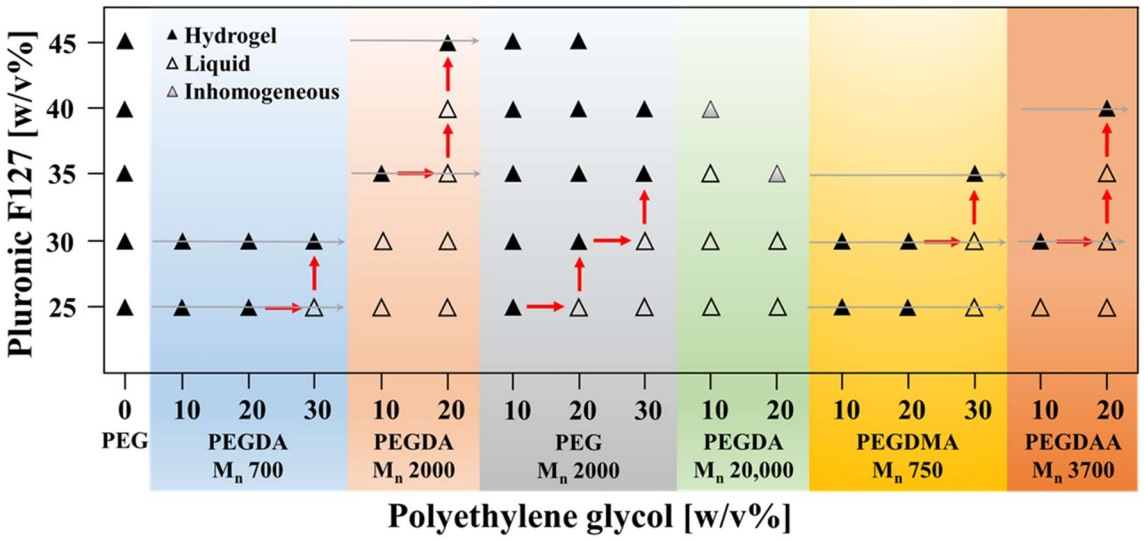

Figure 2: *Binary phase diagram, showing the outcomes of the inverted vial tests for uncrosslinked CPN formulations, at 22 °C as a function of PF127 content at different PEG(DA, DMA, DAA) and PEG with OH end groups, content (uncrosslinked samples). Phase as a function of PEGDA* M_n *was also evaluated. Full and open symbols indicate homogeneous hydrogels and liquids respectively, grey symbols indicate the presence of macroscopic phase separation. Repeats, n=3, were performed for all samples except PEGDA20K, where n=2 repeats both showed phase separation. Photographs of all inverted vial experiments are provided in* ***Figures S2*** *and* ***S3****. The horizontal gey arrows correspond to the series studied in* ***Figure 4****, see text.*

Firstly, for the PEG2K series (with hydroxyl end groups) clear hydrogels formed for 10% PEG at all PF127 content. At 20% PEG a liquid formed at 25% PF127, but higher PF127 content forced gelation, red arrows in ***Figure 2***, grey panel. For 30% PEG, still higher PF127 content, of >30%, was required for gelation. We suggest interaction of PEG chains with the outer PEO groups of the micelles disrupts the micelle-micelle contacts that drive gelation. We will refer to this effect, occurring at higher PEG content, as 'micelle-micelle disruption',[57] see ***Scheme 1A***. The contacts are sufficiently restored by further increasing PF127 content to force gelation.

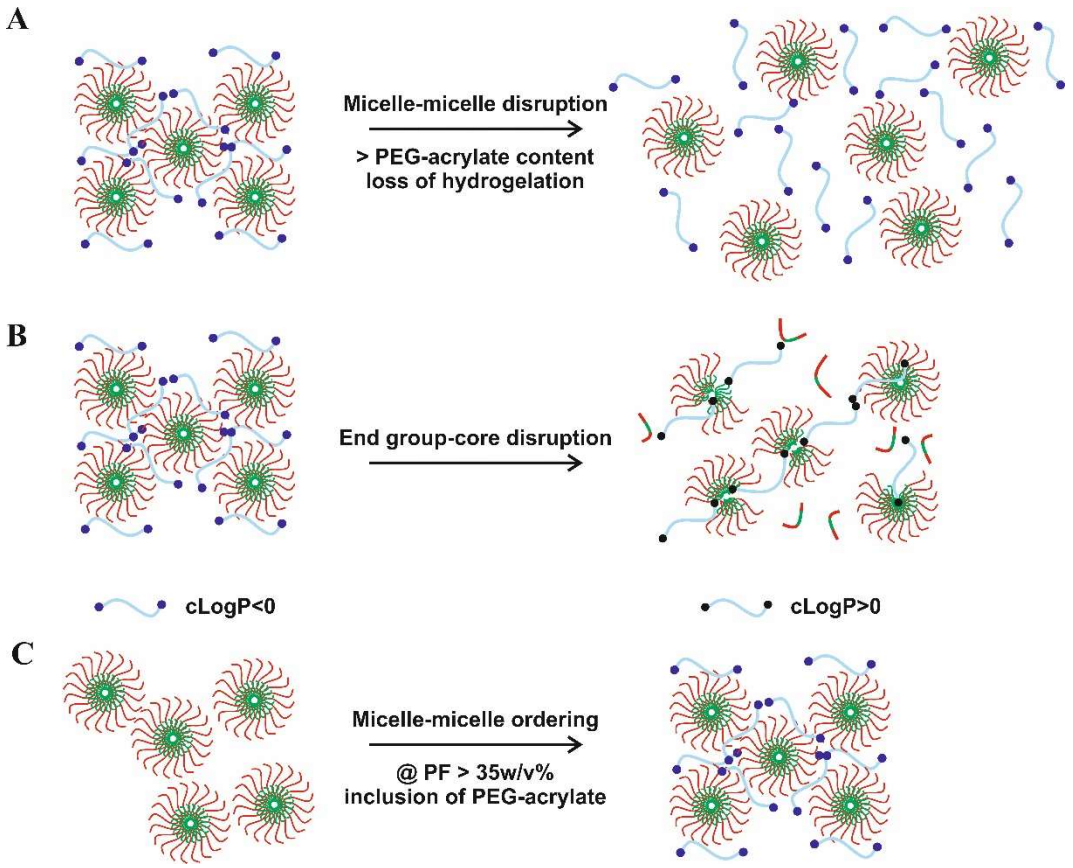

Scheme 1: *Schematic depiction of the effect of inclusion of functionalised-PEG on the network structure of the hydrogels:* ***(A)*** *micelle-micelle disruption;* ***(B)*** *end group-core disruption;* ***(C)*** *micelle-micelle ordering.*

Comparison of the PEGDA700 and PEGDMA750 series (***Figure 2***, blue and orange, respectively) reveals a different effect. Note first that for these two series the end group and chain content, and indeed the chain length and the PEG/PF127 ratio, are all very similar. Gels are formed in all cases at 10 and 20% PEG, while at 30% both series were liquids at low PF127 content. However higher PF127 content was required to force gelation for DMA than for DA, so this disruptive effect depends on end group type. The *clogP* values (partition coefficients, see Methods) of DA and DMA end groups were calculated as positive, at 1.36 and 1.98, respectively, indicating both groups prefer to avoid H_2O. We suggest that these groups interact with the inner PPO block of PF127, disrupting micellisation and hence hydrogelation.[58] We will refer to this as 'end group-core disruption', see ***Scheme 1B***. The effect is reduced by further increasing the PF127 content, with higher PF127 content required for DMA due to stronger core disruption (higher *clogP*).

Micelle-micelle and end group-core disruption are apparent across the study, although the two effects are more difficult to separate for the other pairs of series. Nevertheless, as noted above, for five of the six CPN series studied (red arrows) a PF127 content is identifiable at which gelation was observed at lower but disrupted at higher PEG content. While further increasing PF127 content (at the higher PEG content) produced clear gels. The one exception is PEGDA20K, for which hydrogels did not form. This is probably due to stronger micelle-micelle disruption from the longer chains, as any end group-core disruption must be far weaker, than for example in PEGDA2K, due to the 10-fold lower end group concentration. There is no evidence from this study to suggest that longer chains bridge micelles and so promote gelation. Indeed attempts to force gelation for PEGDA20K by using still higher PF127 content resulted in phase separation, over 24-72 hours. All other formulations remained stable rheologically and for printing, on storing at 4 °C or at RT for at least 30 days (the longest time used).

Increased micelle-micelle disruption due to longer PEG chain length can also be inferred from; (i) higher PF127 content was required for gelation of PEGDA2K than for PEGDA700 (same end group); (ii) for the four hydrogel series with acrylate end groups, those with low M_n (PEGDA700, PEGDMA750) required a 5% increase in PF127 to force gelation, while for higher M_n (PEGDA2K, PEGDAA3.7K) a 10% increase was required, and finally; (iii) for PEGDAA3.7K gelation was at higher PF127 content than for the lower M_n PEG2K series. The end group-core disruption should be minimal for both these series; for DAA *clogP* < 0 indicating preference for water solvation.

In summary, analysis of the phase diagram suggests a delicate balance of cohesive/hydrophobic interactions. The PF127/PEG ratio largely determines the phase, and the gelation composition is dependent on the end group *clogP* (for hydrophobic end groups) and the PEG chain length. Longer chains increase micelle-micelle disruption and decrease end group-core disruption indirectly by dilution. At very high chain length phase cohesion is compromised.

(ii) Structural analysis of CPN hydrogels

We first considered the two pure phases. SAXS scattering patterns of pure PEGDA700, PEGDA2K, PEGDA20K, PEGDMA750 and PEGDAA3.7K, which are liquids at 20 °C for all studied compositions, ***Figure S4A***, were fitted to mass fractal or generalised Gaussian coil form factor models. These fits provided excellent agreement with the data, confirming the expected structure for functionalised, non-crosslinked PEG (***Table S4***) and photo-crosslinked acrylate-PEGs (***Table S5***).[52, 59]

SAXS measurements performed on a series of PF127 hydrogels of ≥25% at 20 °C, yielded characteristic micellar and paracrystalline scattering curves, ***Figure S5***, ***Tables S6*** and ***S7***.[20] The fitted form-factors assume spherical particles, of radius R, arranged in either face-

centred (FCC) or body-centred cubic (BCC) lattices, with random orientation of the paracrystals arising from the initial formulation in solution. The FCC form factor accounted for the region between 0.1 and 1 nm^{-1} in the SAXS curves, providing information about the internal gel structure. Typical behaviour of close to q^{-4} was observed at low q (<0.1 nm^{-1}) for all concentrations indicating the formation of approximately spherical objects, *i.e.* micelles, as expected, ***Figure S5***. For 25PF and 30PF (25 and 30%) there was a broad peak at q *c.*0.7 nm^{-1}, corresponding to inter-micelle interactions.[20, 60] An estimate of the hydrogel mesh size or lattice spacing, d, can be obtained using the Bragg Law, $d = 2\pi/q^*$.[15, 61, 62] With increasing PF127 content the first peak in the pattern progressively shifted to higher q, corresponding to a decrease in lattice spacing, from d 18.0±0.2 nm for 25PF, down to 15.3±0.2 nm for 45PF, ***Table S6***. This is a clear indicator of more densely packed micelles with increasing Pluronic content. For 35PF the appearance of peaks in the scattering curves demonstrated increasing order, *i.e.* paracrystallinity. The ratio of the intensity of each peak to that of the lowest q peak, q^*, (Iq_n/Iq^*), ***Tables S6*** and ***S7***, identifies the FCC phase for 35PF, in agreement with literature for PF127.[20] The FCC phase is also apparent for 40PF, however with an additional peak corresponding to some imperfections in the unit cell.

For all uncrosslinked CPN hydrogels studied SAXS demonstrated crystallinity, ***Figure 3A***. Strong features were present at 30 and even at 25% PF127, which we assign to ordered micelle arrays. For pure PF127 gels features of this type only emerge for ≥35%, ***Figure S5***, so inclusion of PEG makes ordering of the micelle distribution energetically favourable at lower PF content. We will refer to this effect, occurring at lower PEG content in the gel state, as 'micelle-micelle ordering', ***Scheme 1C***. We suggest that by associating with the outer PEO blocks of the micelles the effective size increases, favouring ordered packing. As noted above, at higher PEG content the close balance of cohesive/hydrophobic interactions is altered tipping the system into the liquid phase, ***Figure 2***. We suggest that 'micelle-micelle disruption' occurs

when there is sufficient PEG present that a fraction of it does not directly interact with the outer PEO blocks of the micelles and is free to promote dynamics of chains and micelles.

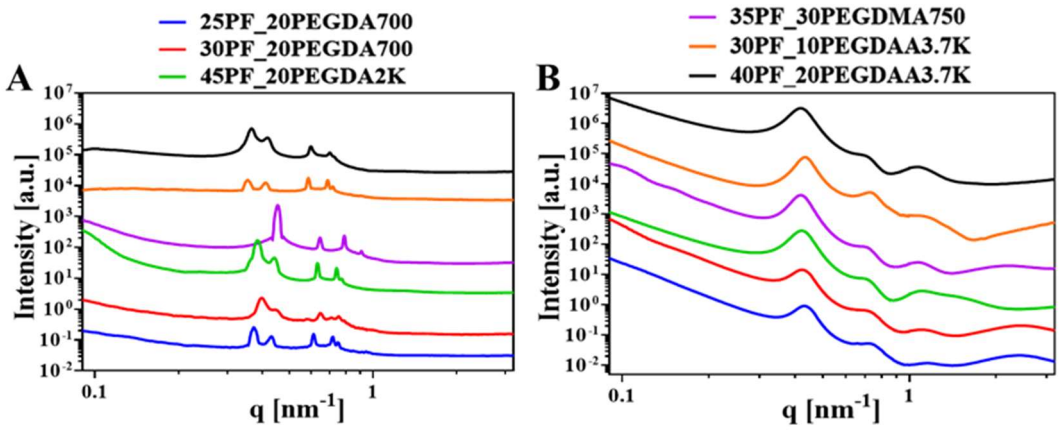

Figure 3: *SAXS patterns, recorded at 20 °C vertically offset for comparison, of* ***(A)*** *uncrosslinked and* ***(B)*** *crosslinked CPN hydrogels, these were fitted to an FCC or BCC form-factor model (see text,* ***Table S8****) and to a power law (****Table 2****).*

The uncrosslinked CPN SAXS curves were all successfully fitted to an FCC model, ***Table 2***, ***Table S8***, except for 35PF_30PEGDMA750 which was fitted to BCC. Interestingly, the BCC phase was also observed at higher content, of 45%, than for pure PF127, which is again consistent with PEG-induced micelle-micelle ordering. Considering the power law fittings, there was significant variation in the power, or fractal, dimension, d_f, values across the series, indicating a wide range of structures in the uncrosslinked state from almost spherical (d_f, 0.03 for 40PF_20PEGDAA3.7K) to ellipsoid (d_f 0.6, 30PF_10PEGDAA3.7K) to mass fractal (d_f 1.5, 25PF_20PEGDA700) to smooth surface fractal (d_f 4.1, 30PF_20PEGDA700 and d_f 4.2, 45PF_20PEGDA2K), ***Table 2***. Despite this variation the characteristic distance, D0, extracted from the power law fits is relatively insensitive to the formulation with values in the 16-18 nm range. For CPN formulations D0 reflects an average separation of the components (PEG and PF127), *i.e.* it is a measure of mesh size.[16] 35PF_30PEGDMA750 is the only

exception, with a lower D0 of 14.1±0.2 nm obtained. We suggest that this very small separation is an end group effect, arising due to the dimethacrylate functionalities (PEGDMA has the highest *clogP* value) which may be exacerbated by the BCC packing in this case. There was a slight decrease in D0 for xPF_20PEGDA700 on increasing PF127 from 25 to 30%, which we ascribe to micelle-micelle ordering on increasing the PEG/PF ratio, *i.e.* for 20PF_20PEGDA700 compared 30PF_20PEGDA700, ***Table 2***. Finally, there was no correlation between the fractal dimension, d_f, and the D0 values across the series.

Table 2. *Power laws (at low q) and first peaks, D0, (showing changes in unit cell size) extracted from the SAXS curves recorded at 20 °C for uncrosslinked (FCC form-factor model) and for crosslinked (power law) CPN hydrogels. Note background colours correspond to the groups in* ***Figure 2****.*

Sample	Uncrosslinked			Crosslinked		
	Power, d_f [a]	Type of d_f	D0 [nm] [b]	Power, d_f	Type of d_f	D0 [nm]
25PF_20PEGDA700	1.5 ± 0.1	Mass fractal	16.3 ± 0.1	3.7 ± 0.1	Rough Surface	14.8 ± 0.2
30PF_20PEGDA700	4.1 ± 0.1	Smooth surface	15.7 ± 0.2	3.5 ± 0.1	Rough Surface	14.9 ± 0.1
45PF_20PEGDA2K	4.2 ± 0.1	Smooth surface	16.3 ± 0.2	3.1 ± 0.1	Rough Surface	15.0 ± 0.2
35PF_30PEGDMA750	2.7 ± 0.1	Rough surface	14.1 ± 0.2	2.9 ± 0.1	Rough surface	15.0 ± 0.2
30PF_10PEGDAA3.7K	0.6 ± 0.1	Ellipsoid	17.8 ± 0.2	3.7 ± 0.1	Rough Surface	15.1 ± 0.1
40PF_20PEGDAA3.7K	0.03 ± 0.1	Spherical	17.1 ± 0.1	2.9 ± 0.1	Rough Surface	15.0 ± 0.1

a. The d_f values were obtained by fitting power laws from 0.0045 – 0.007 Å (corresponding to 90 – 140 nm), except for 35PF_30PEGDMA750 (uncrosslinked) which was fitted from 0.00969 – 0.0154 Å (41 – 65 nm).

b. Scattering curves of uncrosslinked CPN samples were fitted to a face-centred cubic (FCC) phase, apart from 35PF_30PEGDMA750 which was fitted to a body-centred cubic (BCC) phase.

On photo-crosslinking the CPNs the ordered micelle packing was lost and a series of broad peaks was observed, ***Table S8***, ***Table S9***, demonstrating a more amorphous structure.

The low-q region was successfully fitted to a power law (as compared to FCC for uncrosslinked samples). The analysis shows similar d_f values ($2.9 < d_f < 3.7$), corresponding to a rough surface fractal form, in all cases. The D0 values were also all very similar; and in most cases D0 decreased on crosslinking, as expected, ***Table 2***. Hence crosslinking leads to similar structuring (on the 90-140 nm scale), irrespective of the structure prior to irradiation. 35PF_30PEGDMA750 is noteworthy, its uncrosslinked D0 was exceptionally small, as mentioned above, but this relaxed to the norm on crosslinking. It appears that the end group-core disruption is released by converting the free DMA groups (to link PEG moieties outside the cores). This suggests that the final network mesh size, which prior to crosslinking was dictated by contacts between the PF127 micelles, is subsequently determined by the permanently crosslinked PEG network which disrupts micelle ordering, ***Scheme 1A***.

To sum up, at higher content PEG chains disrupt micelle-micelle interactions and PEG end groups disrupt micelle cores, resulting in liquids. At lower content PEG forces micelle ordering within the gels in which cases, despite the large variation in structures formed, the separation of the two components is very similar. This suggests that there may be potential to use the chain length and end group type to provide appropriate rheological properties for printing and to alter the degradation profiles, while capturing similar final network characteristics (*e.g.* mesh size).

(iii) Temperature dependent gelation and rheology of CPN hydrogels

Sections (i) and (ii) show that composition determines CPN structure and local dynamics in the resting state. These factors undoubtedly influence the formulations response under shear, and so may affect printability. First the effects on critical gelation temperature, CGT, and critical gelation concentration, CGC, were evaluated. The temperature dependence of gelation for the different series of formulations was studied by measuring viscosity, η, across

the accessible printing window of 20-30 °C. A parallel plate geometry was employed at low shear rate, $\dot{\gamma}$, of 0.1 s^{-1}, all the data are provided in ***Figures S6***. Considering pure Pluronic; for 25PF a significant decrease in η was observed on decreasing temperature from 22 to 20 °C ($p<0.001$), ***Figure 4A*** and **inset**, corresponding to the expected changes leading to the gel-to-sol transition below room temperature. For 30PF the higher Pluronic content shifted the CGT to below our studied temperature range, as was also noted by Kushan and Senses.[42]

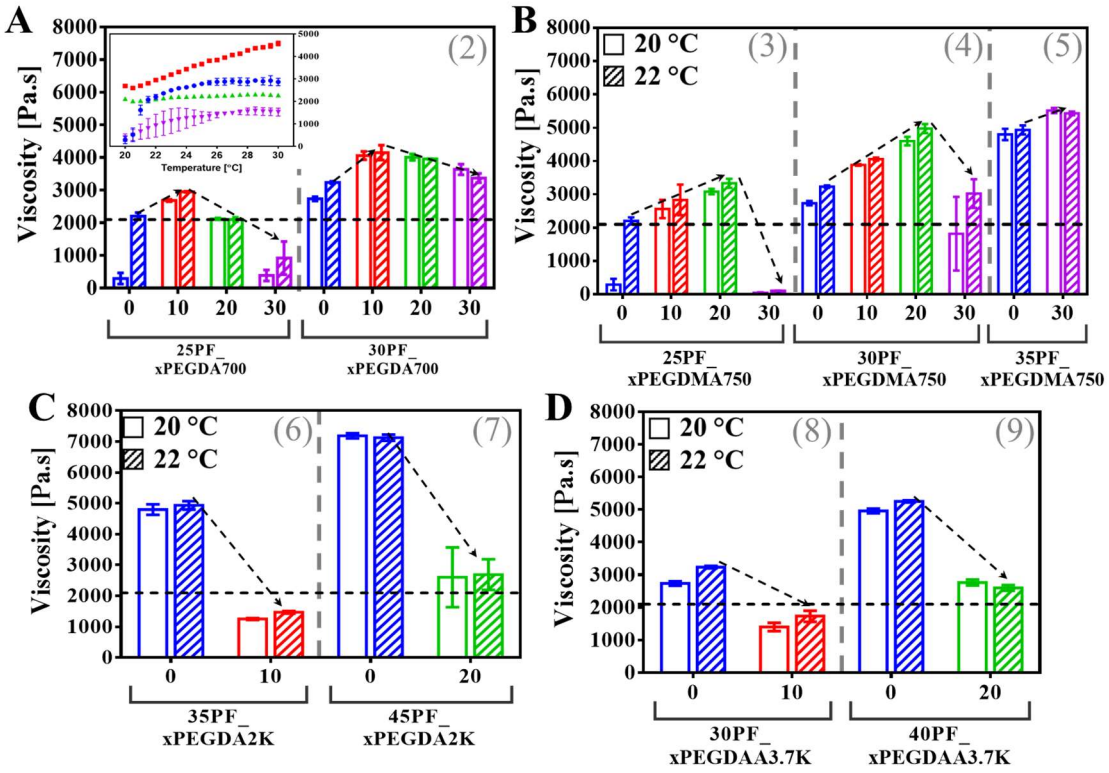

Figure 4: *Viscosity, η, as a function of composition recorded at 20 (empty columns) and 22°C (filled columns) extracted from temperature sweep measurements, at shear rate, $\dot{\gamma}$ = 0.1 s^{-1}, for uncrosslinked CPNs.* ***(A)*** *xPF_yPEGDA700, with inset an example full temperature sweep for 25PF_yPEGDA700,* ***(B)*** *xPF_yPEGDMA750,* ***(C)*** *xPF_yPEGDA2K, and* ***(D)*** *xPF_yPEGDAA3.7K. n=2 repeats measurements were performed, the error bars represent the ranges, in some cases these are smaller than the data mark sizes. The horizontal dashed line is η = 2100 Pa.s, indicating the lower edge, from our experience, of the printable range, see*

text. All formulations with $\eta < 2100$ *Pa.s are liquids at that temperature; these correspond to the* Δ *markers in* ***Figure 2****.*

We turn next to the CPN formulations, focusing again on the temperature range from 22 to 20 °C (around lab temperature), in which the changes were very strong and because this is an easily accessible printing range. Note that the data series labelled (1)-(9) in ***Figure 4*** correspond to the nine sets of CPN formulations indicated by grey lines in ***Figure 2***. First considering xPF_yPEGDA700, ***Figure 4A***. For 25% PF127 on including 10% PEGDA700 η increased and gels were formed at both temperatures, with the CGT presumably shifting to below the studied range, ***Figure S6A***. From a practical perspective this shift is very useful as the CPNs remain printable between 20-30 °C, see below. On cooling, the PPO chains are known to disentangle and eventually hydrate.[63] We suggest that micelle-micelle ordering (apparent from SAXS at relatively low PF127 content when PEG in this M_n range is included), enhances gel phase-stability to lower temperature. Further increases in PEG content resulted in a decrease in η due to increased micelle-micelle and end group-micelle disruption, with a η_{max} value apparent at intermediate content. On increasing the PF127 content to 30% similar effects were observed; inclusion of PEG at low content induced further gel stiffening and at higher content distinct slackening, ***Figure 4A***. Interestingly the η_{max} was observed at the same PEG content of 10%, as for 25% PF127, although the dependence on PEG content was weaker, suggesting a predominant role of micelle content. As the number of micelles increases there is proportionately less PEG available for disruption. This is particularly clear for 25PF_30PEGDA700, as compared to 30PF_30PEGDA700, ***Figures 4A*** purple and ***S6B***.

For the xPF_yPEGDMA750 series, ***Figures 4B***, ***S6C-E***, very similar effects to PEGDA were observed, as expected given the similarity in M_n. Interestingly the η_{max} was observed at higher PEG content, of 20%. The decrease in η at higher PEGDMA750 content was also

greater and its onset more sudden, suggesting greater core disruption due to the higher *clogP* end group used. To complete the picture, measurements were undertaken for 35PF_30PEGDMA750, *i.e.* at higher content of both components. The higher micelle to PEG ratio ensured high viscosity was retained despite the presence of a significant fraction of this strong disruptor, again the relative content of micelles and disruptors determines the viscosity and gelation.

Series of formulations were also prepared using PEGDA2K, ***Figures 4C***, ***S6F-G***, and PEGDAA3.7K, ***Figures 4D***, ***S6H-I***, with similar composition-dependent trends in gelation and viscosity observed. For PEGDA2K higher PF127 content, of 35 or 40%, was required to force gelation, and this was significantly disrupted even at 10% PEG. Comparison with 25PF_10PEGDA700 shows that this is primarily due to chain length-dependent micelle-micelle disruption, as the end group content is reduced by ~2.85 times. A very similar effect was seen for PEGDAA3.7K, ***Figure 4D***, for which the end groups should be non-disruptive. As noted above, Kushan and Senses have demonstrated that when nanocompositing PF127 with hydrophilic cellulose nanocrystals (CNC); low CNC content (1-3 wt%) leads to disruption of the micelles and makes the gels much softer and more flexible, while; higher CNC contents (4-5 wt%) leads to the formation of a more dominant CNC network that adds toughness with progressively less disruption of micellisation.[42] This was attributed to trapping of PF127 in a secondary CNC network, which is apparently not a feature of our uncrosslinked gel systems. It is interesting that when nanocompositing PF127 with PEG we observed the reverse composition dependent trend; thickening at lower and slackening at higher content.

This analysis shows that by varying the composition, chain length and end group type the delicate balance of cohesive/hydrophobic interactions can be shifted, tuning the emergent rheological properties. In the next section we will evaluate how these changes impact print quality and whether this can be controlled.

(iv) CPN hydrogel rheological properties and printability

In 3D extrusion printing the inks usually start from a resting state, undergo a structural transition due to high shear while passing through the nozzle, and then re-establish the resting state on deposition.[3] The key rheological properties affecting these changes are viscosity, viscoelastic shear moduli, elastic recovery, and shear stress, as shown schematically in ***Figure 5A***. However, as most of these factors are dynamic their impact on the outcome will also depend on printing conditions, including barrel and needle temperature, extrusion pressure and head velocity.[3] Paxton *et al.* described methods for assessing printability of Pluronic-based gels and reported rheological evaluation of inks to characterise the yield point, shear thinning and recovery behaviour.[14]

Here printability of the five single component PF127, and the fourteen CPN formulations (that include acrylates or acrylamides) which formed gels, was evaluated at 22 °C, the temperature used for rheology and for determining the phase diagram. Our interest was in evaluating printability in terms of composition-dependent rheology. So to quantify CPN properties the flow curves (dependence of viscosity at 22 °C on shear rate), ***Figure S7***, were next fitted to a power law, following Paxton *et al.* [14] (equation 1, Methods). Successful fitting provided consistency (K) values and shear-thinning exponents (n). The % recovery (χ) of the η value was also determined from the flow recovery data, ***Figure S8*** and ***Table S10***, for the first time in the case of pure PF127. Note that the K value is a viscosity at a shear rate of 1 s^{-1},[3] which is a higher rate than used in the experiments shown in ***Figure 4***, so as expected, the extracted K parameters are lower than the measured η values. Although we noticed small discrepancies between the viscosities extracted from the two measurement methods, *i.e.* from temperature sweep and from flow curves recorded using the same parameters of $\dot{y} = 0.1$ s^{-1} and at 22 °C, ***Figure S9***, the overall trends across all formulations persisted. This enables evaluation of the outcomes in terms of the composition-dependent materials parameters (K, n and χ).

Simple grid patterns, shown in ***Figure 5C*** for 30PF_yPEGDA700, were produced using a cylindrical 152 μm (ID) needle. Printability was evaluated by measuring the average feature, or line, thickness, which under ideal conditions should be close to the ID. Printing parameters, thickness values and images are provided in ***Table 1***, ***Table S11*** and ***Figures S10-11***, respectively. We note that all measurements were taken within ~1.5 min of printing to eliminate any time-dependent drying, see Methods.

First the effects of extrusion pressure and velocity are shown for one case, 30PF_10PEGDA700, in ***Figure 5D***. The behaviour was as expected; (i) when higher pressure was used thinner lines were obtained by increasing the velocity and this effect weakened for lower pressure (this is observed for all fifteen CPN series, ***Table S11***), and similarly; (ii) when lower velocity was used thinner lines were obtained by reducing the pressure (this was observed in eleven cases, and the remainder are marginal). Despite this consistency, the sweet spot in parameter space remains difficult to predict.

Next, we evaluated the effect of composition-dependent materials parameters (K, n and χ) on the printing thickness, representative images are shown in ***Figure 5C***. The K values and line thickness are cross-plotted in ***Figure 5E*** for four series; 25PF_yPEGDA700 (blue); 25PF_yPEGDMA750 (green); 30PF_yPEGDA700 (red), and; 30PF_yPEGDMA750 (orange), with fixed printing parameters of Δp 3.17 bar, ν 1000 mm.min^{-1}. The effect of increasing PF127 content was primarily to increase K, which reduced line thickness. This was observed for all possible pairwise comparisons in the library (black arrows in ***Figure 5E***). This trend was also observed for all combinations of printing parameters studied, ***Figure S12***, ***Table S11***. On the other hand, the effect of PF127 on both n and on χ was inconsistent from formulation to formulation for a given printing condition, *i.e.* the consistent trends shown in ***Figure 5E*** between pairs of formulations are not present in ***Figures S12A***, ***B***. Furthermore, these latter trends changed once the printing conditions were altered, ***Figure S12C-E***. Overall, correlation

of rheological properties (K, n and χ) with line thickness of printed features indicates that K is the most sensitive formulation-dependent parameter reducing line thickness at higher values, while the effects on n and χ are inconsistent and less predictable.

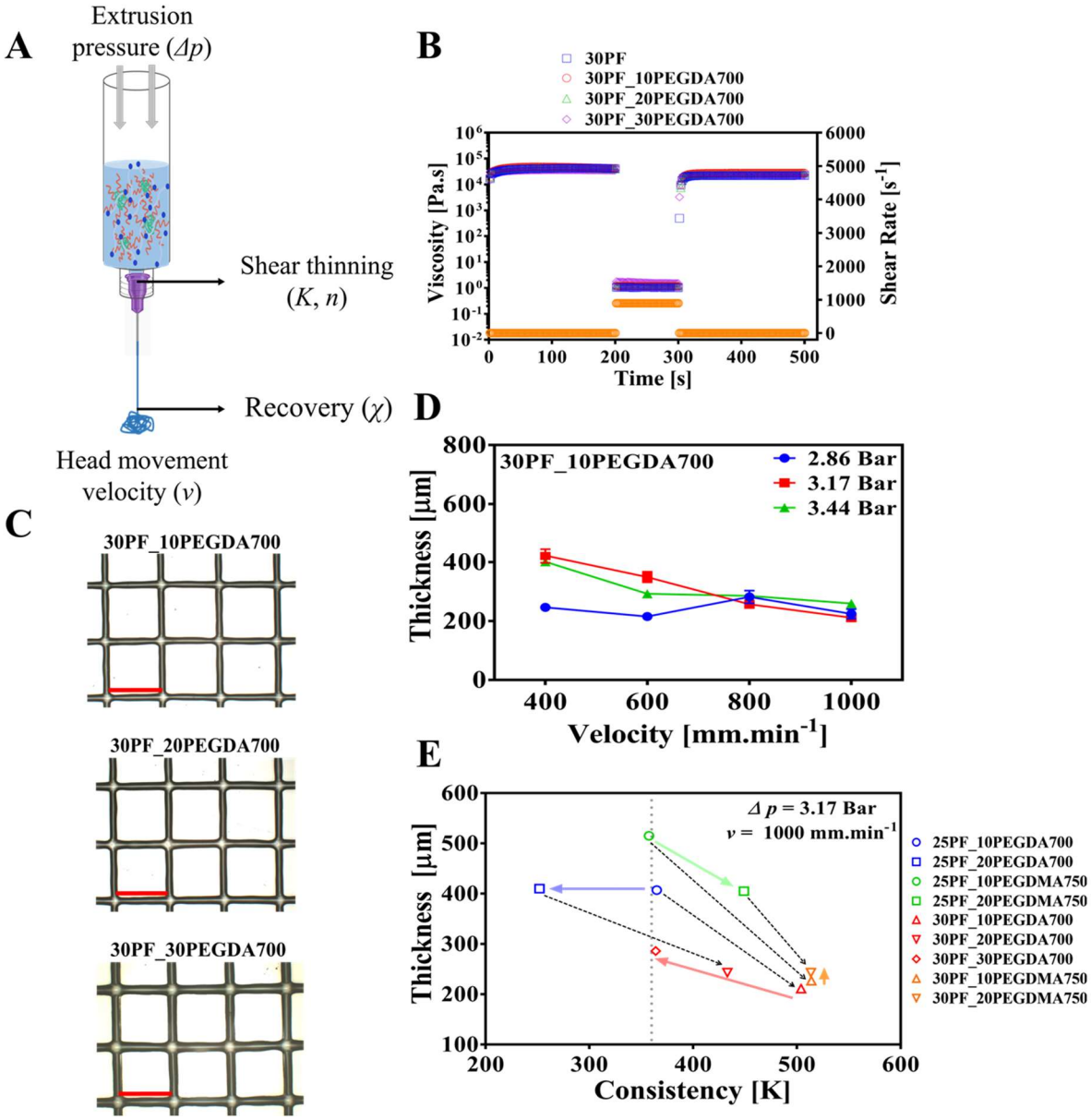

Figure 5: *Effects of composition / rheological properties on printability and fidelity of printed structures.* ***(A)*** *Schematic representation of 3D printing, indicating the role of the printing parameters and CPN properties.* ***(B)*** *Rotational recovery experiments at 22°C with varied concentrations of 30 w/v% PF127 with increasing concentrations of PEGDA M_n 700.* ***(C)***

Comparison of grids printed using pressure 3.17 bar and velocity 1000 mm min^{-1} for the 25PF_yPEGDA700 series, the red scale bar indicates 1.5 mm. ***(D)*** *Effect of printing parameters on feature thickness for the same series.* ***(E)*** *Thickness of grids printed at pressure of 3.17 bar and velocity of 1000 mm min^{-1} as a function of consistency K, for the four series, see* ***Tables S10****,* ***S11*** *and* ***Figures S****7,* ***S8*** *and* ***S12****.*

The effects of increasing PEG content varied across the 30PF_yPEGDA700 (red) series but were independent of the printing parameters. Changing the end group from PEGDA700 to PEGDMA750 consistently led to an increase in K and χ, but a decrease in n. In terms of performance, the thinnest lines achieved were for 30PF_yPEGDA700. We obtained; *(i)* 211 ± 7 μm for 30PF_10PEGDA700 at 3.17 bar pressure and 1000 mm min^{-1} head velocity; *(ii)* 215 ± 10 μm for the same formulation at 2.89 bar and 600 mm min^{-1}, and; *(iii)* 224 ± 9 μm at 3.44 bar and 1000 mm min^{-1} for 30PF_20PEGDA700. In all cases conditions could be identified that provide line thickness no worse than *c.*40% greater than the needle ID.

(v) Photo-crosslinking and 3D printing of higher order structures

CPNs were photo-crosslinked to stabilise selected printed structures. As expected, the UV exposure significantly increased the materials stiffness and resulted in retention of fidelity. The extent of change was clearly dependent on the sample thickness and PEG content. Typically, 1 min of UV exposure was sufficient, but some formulations with lower acrylate content did not fully crosslink even with extended time, ***Table S3***. The mechanical stiffness at 22 °C of 25PF_20PEGDA700, selected as it gave good line thickness and appeared to fully crosslink, was measured using oscillatory rheology, ***Figure 6A***. A significant increase in storage modulus was observed ($p<0.001$) from 10.0 ± 0.2 to 74.3 ± 1.7 kPa for the crosslinked (CL) as compared to the uncrosslinked (UCL) print. Rheological measurements for multiple

formulations confirmed this outcome. 5 minutes of crosslinking typically resulted in 3- to 7-fold increases in storage modulus, ***Figure S13***. For several samples that appeared to the eye to be fully converted, extending the irradiation time provided no further increase in G'.

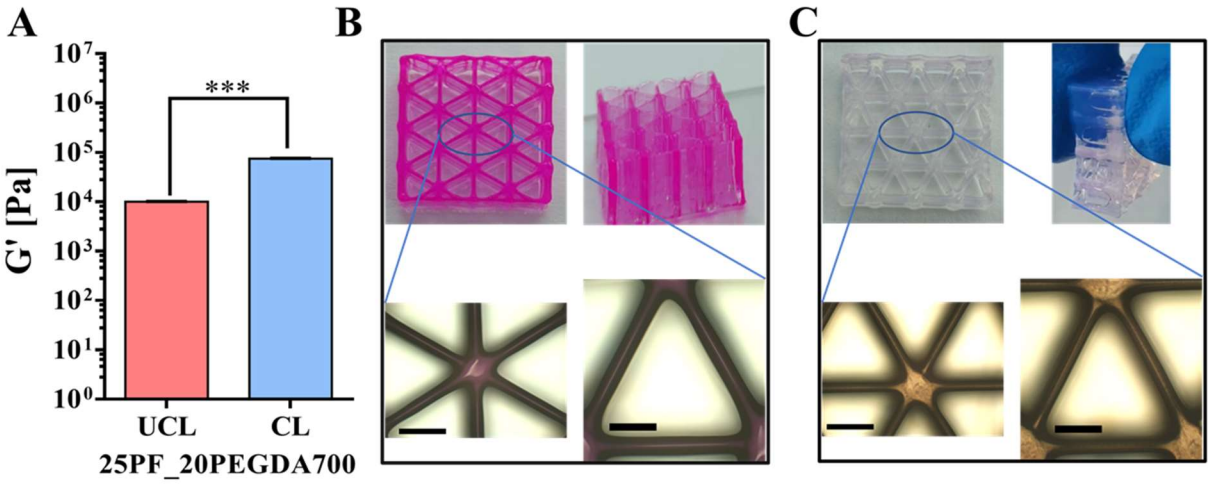

***Figure 6**: **(A)** Storage modulus, measured at 22 °C, for 25PF_20PEGDA700 CPN uncrosslinked (UCL), and crosslinked (CL) for 1 min under 365 nm UV light at 16 mW power (n=2), *** p<0.001. Representative complex structures printed using 25PF_20PEGDA700 **(B)** uncrosslinked, which **(C)** was subsequently crosslinked. The scale bars indicate 1.5 mm.*

For the 25PF_20PEGDA700 experiment excellent smoothness and good line thickness of 246 ± 9 µm was obtained at 2.86 bar and 1000 mm min^{-1}. The formulation was coloured using Nile red dye, at a concentration of 0.002 w/v% for visualisation prior to UV crosslinking, which unfortunately bleached the colour. Nevertheless, on crosslinking the line thickness decreased to 203 ± 14 µm, and encouragingly the junctions and gross structure were both unchanged despite the increase in stiffness.

Finally, the integrity of both uncrosslinked and crosslinked printed structures in water at 20 °C, was evaluated. Representative 25PF_20PEGDA700 prints were placed in 5 mL of water, sufficient to fully submerge them, see ***Supporting movies SM1*** and ***SM2***, for the uncrosslinked and crosslinked responses, respectively. The uncrosslinked print could not be

picked up using a spatula and was observed to dissolve within minutes. The crosslinked print retained its integrity and could be easily lifted. The crosslinked prints retained fidelity for at least for a month in water at 20 °C, after a week they started to shrink if not kept in water, but when water was subsequently added they rehydrated (swelled) and recovered their original printed shape without any signs of breakage.

Conclusions

Measurements of the composition dependence of gelation and internal structuring of CPN networks, and of their dynamical responses to shear provide insight into the interactions determining micellization, assembly, and flow. A picture emerges of a fine, PEG/PF127 composition-dependent, balance between cohesive and disruptive interactions, modulated by chain length and end group type. Low PEG content forces micelle ordering at lower micelle content than for pure PF127, we suggest that persistent associations between the PEG and micelle surfaces extend the length scale of inter-micelle interactions, and this also increases viscosity. At higher PEG content micelles are disrupted by the acrylate end groups and viscosity decreases due to an increasing fraction of non-associated PEG, which increases local dynamics and disrupts gelation. By varying PEG chain length and end group it may be possible to both adjust the rheology and determine the degradation.

The effect of PF127 content on printability is found to be predictable; with increasing content the consistency, K, increases and line thickness decreases. On the other hand, the effect of PEG is unpredictable but independent of the printing conditions, reflecting complex interplay of end group- and chain length-dependent effects. The analysis suggests that rational design may be possible when compositing CPN networks that include supramolecular assemblies. On the other hand, brute-force optimisation may be needed to determine optimal composition of molecular ink components, which do not have intermediate scale order. There

may be a role for machine learning in predicting optimal printing conditions for supramolecular/molecular composite inks, once larger training datasets become available.

Supplementary information

The following file is available free of charge:

Supporting method, modelling description and discussion of SAXS; Additional SAXS data graphs and Tables; Additional Photographs depicting inks/hydrogels phases; Additional rheological characterisation of inks/hydrogel formulations; Additional photographs and tables depicting printability study for remaining formulations; Table describing UV-crosslinking study observation and times; G-codes used for printing of the structures. Rheological assessment of crosslinked formulations. Supporting Movies showing degradation of uncrosslinked and crosslinked formulation placed in H_2O.

Funding sources

The authors acknowledge support from Science Foundation Ireland (16/IA/4584). We would like to thank to Diamond Light Source for the Beam Time Award (SM28287) to J.K.W. and C.J.C. E-G..

Acknowledgements

We would like to thank Clara Zehe and Gareth Redmond for their support with the optical microscopy imaging. We would like to thank Kevin M^{c}Carthy, Ross Lawless and Valdemaras Abromaitis for their assistance with the design and wiring of the UV ring.

Notes

The authors declare no competing financial interest. All research data supporting this publication are directly available within this publication and associated supporting information.

ORCID numbers of authors:

Krutika Singh: https://orcid.org/0000-0002-7016-1542

Jacek K. Wychowaniec: https://orcid.org/0000-0002-6597-5242

Charlotte J. C. Edwards-Gayle: https://orcid.org/0000-0001-7757-107X

Emmanuel G. Reynaud: https://orcid.org/0000-0003-1502-661X

Brian J. Rodriguez: https://orcid.org/0000-0001-9419-2717

Dermot Brougham: https://orcid.org/0000-0002-1270-8415

References

[1] J. Malda, J. Visser, F.P. Melchels, T. Jüngst, W.E. Hennink, W.J.A. Dhert, J. Groll, D.W. Hutmacher, 25th Anniversary Article: Engineering Hydrogels for Biofabrication, Advanced Materials 25(36) (2013) 5011-5028.

[2] J.K. Wychowaniec, D.F. Brougham, Emerging Magnetic Fabrication Technologies Provide Controllable Hierarchically-Structured Biomaterials and Stimulus Response for Biomedical Applications, Advanced Science n/a(n/a) (2022) 2202278.

[3] A. Schwab, R. Levato, M. D'Este, S. Piluso, D. Eglin, J. Malda, Printability and Shape Fidelity of Bioinks in 3D Bioprinting, Chemical Reviews (2020).

[4] O. Chaudhuri, J. Cooper-White, P.A. Janmey, D.J. Mooney, V.B. Shenoy, Effects of extracellular matrix viscoelasticity on cellular behaviour, Nature 584(7822) (2020) 535-546.

[5] G.B. Chen, C.J. Dong, L. Yang, Y. Lv, 3D Scaffolds with Different Stiffness but the Same Microstructure for Bone Tissue Engineering, ACS Appl. Mater. Interfaces 7(29) (2015) 15790-15802.

[6] T. Kivijärvi, G. Øyvind, M.A. Yassin, S. Jain, S. Yamada, A. Morales-López, K. Mustafa, A. Finne-Wistrand, Hybrid material based on hyaluronan hydrogels and poly(l-lactide-co-1,3-trimethylene carbonate) scaffolds toward a cell-instructive microenvironment with long-term in vivo degradability, Materials Today Bio 17 (2022) 100483.

[7] K.R. Stevens, J.S. Miller, B.L. Blakely, C.S. Chen, S.N. Bhatia, Degradable hydrogels derived from PEG-diacrylamide for hepatic tissue engineering, Journal of Biomedical Materials Research Part A 103(10) (2015) 3331-3338.

[8] M.B. Browning, E. Cosgriff-Hernandez, Development of a Biostable Replacement for PEGDA Hydrogels, Biomacromolecules 13(3) (2012) 779-786.

[9] M.B. Browning, S.N. Cereceres, P.T. Luong, E.M. Cosgriff-Hernandez, Determination of the in vivo degradation mechanism of PEGDA hydrogels, Journal of Biomedical Materials Research Part A 102(12) (2014) 4244-4251.

[10] Z. Zhao, C. Vizetto-Duarte, Z.K. Moay, M.I. Setyawati, M. Rakshit, M.H. Kathawala, K.W. Ng, Composite Hydrogels in Three-Dimensional in vitro Models, Frontiers in Bioengineering and Biotechnology 8 (2020) 611.

[11] N.J. Treacy, S. Clerkin, J.L. Davis, C. Kennedy, A.F. Miller, A. Saiani, J.K. Wychowaniec, D.F. Brougham, J. Crean, Growth and differentiation of human induced pluripotent stem cell (hiPSC)-derived kidney organoids using fully synthetic peptide hydrogels, Bioactive Materials 21 (2023) 142-156.

[12] C.M. Walsh, J.K. Wychowaniec, L. Costello, D.F. Brougham, D. Dooley, An In Vitro and Ex Vivo Analysis of the Potential of GelMA Hydrogels as a Therapeutic Platform for Preclinical Spinal Cord Injury, Advanced Healthcare Materials (2023) 2300951.

[13] C.M. Walsh, J.K. Wychowaniec, D.F. Brougham, D. Dooley, Functional hydrogels as therapeutic tools for spinal cord injury: New perspectives on immunopharmacological interventions, Pharmacology & Therapeutics 234 (2022) 108043.

[14] N. Paxton, W. Smolan, T. Böck, F. Melchels, J. Groll, T. Jungst, Proposal to assess printability of bioinks for extrusion-based bioprinting and evaluation of rheological properties governing bioprintability, Biofabrication 9(4) (2017) 044107.

[15] J.K. Wychowaniec, A.M. Smith, C. Ligorio, O.O. Mykhaylyk, A.F. Miller, A. Saiani, Role of Sheet-Edge Interactions in β-sheet Self-Assembling Peptide Hydrogels, Biomacromolecules 21(6) (2020) 2285-2297.

[16] B. Wu, W. Chassé, R. Peters, T. Brooijmans, A.A. Dias, A. Heise, C.J. Duxbury, A.P.M. Kentgens, D.F. Brougham, V.M. Litvinov, Network Structure in Acrylate Systems: Effect of Junction Topology on Cross-Link Density and Macroscopic Gel Properties, Macromolecules 49(17) (2016) 6531-6540.

[17] J. Gao, C. Tang, A.M. Smith, A.F. Miller, A. Saiani, Controlling self-assembling peptide hydrogel properties through network topology, Biomacromolecules (2017).

[18] A.P. Dhand, J.H. Galarraga, J.A. Burdick, Enhancing Biopolymer Hydrogel Functionality through Interpenetrating Networks, Trends in Biotechnology 39(5) (2021) 519-538.

[19] A. Ribeiro, M.M. Blokzijl, R. Levato, C.W. Visser, M. Castilho, W.E. Hennink, T. Vermonden, J. Malda, Assessing bioink shape fidelity to aid material development in 3D bioprinting, Biofabrication 10(1) (2017) 014102.

[20] B. Shriky, A. Kelly, M. Isreb, M. Babenko, N. Mahmoudi, S. Rogers, O. Shebanova, T. Snow, T. Gough, Pluronic F127 thermosensitive injectable smart hydrogels for controlled drug delivery system development, Journal of Colloid and Interface Science 565 (2020) 119-130.

[21] M. Bohorquez, C. Koch, T. Trygstad, N. Pandit, A Study of the Temperature-Dependent Micellization of Pluronic F127, Journal of Colloid and Interface Science 216(1) (1999) 34-40.

[22] P.A.N.S. Priyadharshana, J.-Y. Park, S.-H. Hong, J.-K. Song, Multiresponsive Polymer Nanocomposite Liquid Crystals Having Heterogeneous Phase Transitions for Battery-Free Temperature Maintenance Indicators, Small 18(38) (2022) 2203551.

[23] P.T. Smith, A. Basu, A. Saha, A. Nelson, Chemical modification and printability of shear-thinning hydrogel inks for direct-write 3D printing, Polymer 152 (2018) 42-50.

[24] Y.-s. Jung, W. Park, H. Park, D.-K. Lee, K. Na, Thermo-sensitive injectable hydrogel based on the physical mixing of hyaluronic acid and Pluronic F-127 for sustained NSAID delivery, Carbohydrate Polymers 156 (2017) 403-408.

[25] H.-R. Lin, K.C. Sung, W.-J. Vong, In Situ Gelling of Alginate/Pluronic Solutions for Ophthalmic Delivery of Pilocarpine, Biomacromolecules 5(6) (2004) 2358-2365.

[26] C.-J. Wu, A.K. Gaharwar, B.K. Chan, G. Schmidt, Mechanically Tough Pluronic F127/Laponite Nanocomposite Hydrogels from Covalently and Physically Cross-Linked Networks, Macromolecules 44(20) (2011) 8215-8224.

[27] H.-W. Kang, S.J. Lee, I.K. Ko, C. Kengla, J.J. Yoo, A. Atala, A 3D bioprinting system to produce human-scale tissue constructs with structural integrity, Nature Biotechnology 34(3) (2016) 312-319.

[28] D.B. Kolesky, R.L. Truby, A.S. Gladman, T.A. Busbee, K.A. Homan, J.A. Lewis, 3D Bioprinting of Vascularized, Heterogeneous Cell- Laden Tissue Constructs, Advanced Materials 26(19) (2014) 3124-3130.

[29] D.B. Kolesky, K.A. Homan, M.A. Skylar-Scott, J.A. Lewis, Three-dimensional bioprinting of thick vascularized tissues, Proceedings of the National Academy of Sciences 113(12) (2016) 3179.

[30] H. Arslan, A. Nojoomi, J. Jeon, K. Yum, 3D Printing of Anisotropic Hydrogels with Bioinspired Motion, Advanced Science 6(2) (2019) 1800703.

[31] M. Müller, J. Becher, M. Schnabelrauch, M. Zenobi-Wong, Nanostructured pluronic hydrogels as bioinks for 3d bioprinting, Biofabrication 7(3) (2015) 035006.

[32] E. Rani Aluri, E. Gannon, K. Singh, S. Kolagatla, K. Kowiorski, S. Shingte, E. McKiernan, C. Moloney, K. McGarry, L. Jowett, B.J. Rodriguez, D.F. Brougham, J.K. Wychowaniec,

Graphene oxide modulates inter-particle interactions in 3D printable soft nanocomposite hydrogels restoring magnetic hyperthermia responses, Journal of Colloid and Interface Science 611 (2022) 533-544.

[33] H.H. Jung, K. Park, D.K. Han, Preparation of TGF-β1-conjugated biodegradable pluronic F127 hydrogel and its application with adipose-derived stem cells, Journal of Controlled Release 147(1) (2010) 84-91.

[34] Y.-J. Jang, S.Y. Chun, G.N. Kim, J.R. Kim, S.H. Oh, J.H. Lee, B.S. Kim, P.H. Song, E.S. Yoo, T.G. Kwon, Characterization of a novel composite scaffold consisting of acellular bladder submucosa matrix, polycaprolactone and Pluronic F127 as a substance for bladder reconstruction, Acta Biomaterialia 10(7) (2014) 3117-3125.

[35] I.M.A. Diniz, C. Chen, X. Xu, S. Ansari, H.H. Zadeh, M.M. Marques, S. Shi, A. Moshaverinia, Pluronic F-127 hydrogel as a promising scaffold for encapsulation of dental-derived mesenchymal stem cells, Journal of materials science. Materials in medicine 26(3) (2015) 153-153.

[36] R. Jaquilin P J, O.S. Oluwafemi, S. Thomas, A.O. Oyedeji, Recent advances in drug delivery nanocarriers incorporated in temperature-sensitive Pluronic F-127–A critical review, Journal of Drug Delivery Science and Technology 72 (2022) 103390.

[37] I. Swennen, V. Vermeersch, M. Hornof, E. Adriaens, J.P. Remon, A. Urtti, E.H. Schacht, In-situ crosslinkable thermo-responsive hydrogels for drug delivery, Journal of Controlled Release 116(2) (2006) e21-e24.

[38] S.H. Lee, Y. Lee, S.-W. Lee, H.-Y. Ji, J.-H. Lee, D.S. Lee, T.G. Park, Enzyme-mediated cross-linking of Pluronic copolymer micelles for injectable and in situ forming hydrogels, Acta Biomaterialia 7(4) (2011) 1468-1476.

[39] S. Chatterjee, P.C.-l. Hui, C.-w. Kan, W. Wang, Dual-responsive (pH/temperature) Pluronic F-127 hydrogel drug delivery system for textile-based transdermal therapy, Scientific Reports 9(1) (2019) 11658.

[40] J. García-Couce, M. Tomás, G. Fuentes, I. Que, A. Almirall, L.J. Cruz, Chitosan/Pluronic F127 Thermosensitive Hydrogel as an Injectable Dexamethasone Delivery Carrier, Gels 8(1) (2022) 44.

[41] J. Cao, M. Su, N. Hasan, J. Lee, D. Kwak, D.Y. Kim, K. Kim, E.H. Lee, J.H. Jung, J.-W. Yoo, Nitric Oxide-Releasing Thermoresponsive Pluronic F127/Alginate Hydrogel for Enhanced Antibacterial Activity and Accelerated Healing of Infected Wounds, Pharmaceutics 12(10) (2020) 926.

[42] E. Kushan, E. Senses, Thermoresponsive and Injectable Composite Hydrogels of Cellulose Nanocrystals and Pluronic F127, ACS Applied Bio Materials 4(4) (2021) 3507-3517.

[43] P.T. Luong, M.B. Browning, R.S. Bixler, E. Cosgriff-Hernandez, Drying and storage effects on poly(ethylene glycol) hydrogel mechanical properties and bioactivity, Journal of Biomedical Materials Research Part A 102(9) (2014) 3066-3076.

[44] L. Lin, J. Zhu, K. Kottke-Marchant, R.E. Marchant, Biomimetic-Engineered Poly (Ethylene Glycol) Hydrogel for Smooth Muscle Cell Migration, Tissue Engineering Part A 20(3-4) (2013) 864-873.

[45] X. Cui, K. Breitenkamp, M.G. Finn, M. Lotz, D.D. D'Lima, Direct Human Cartilage Repair Using Three-Dimensional Bioprinting Technology, Tissue Engineering Part A 18(11-12) (2012) 1304-1312.

[46] L.A. Hockaday, K.H. Kang, N.W. Colangelo, P.Y.C. Cheung, B. Duan, E. Malone, J. Wu, L.N. Girardi, L.J. Bonassar, H. Lipson, C.C. Chu, J.T. Butcher, Rapid 3d printing of anatomically accurate and mechanically heterogeneous aortic valve hydrogel scaffolds, Biofabrication 4(3) (2012) 035005.

[47] N.A. Sears, T.S. Wilems, K.A. Gold, Z. Lan, S.N. Cereceres, P.S. Dhavalikar, R. Foudazi, E.M. Cosgriff-Hernandez, Hydrocolloid Inks for 3D Printing of Porous Hydrogels, Advanced Materials Technologies 4(2) (2019) 1800343.

[48] X. Zhou, M. Nowicki, H. Cui, W. Zhu, X. Fang, S. Miao, S.J. Lee, M. Keidar, L.G. Zhang, 3D bioprinted graphene oxide-incorporated matrix for promoting chondrogenic differentiation of human bone marrow mesenchymal stem cells, Carbon 116 (2017) 615-624.

[49] M. Choi, J.W. Choi, S. Kim, S. Nizamoglu, S.K. Hahn, S.H. Yun, Light-guiding hydrogels for cell-based sensing and optogenetic synthesis in vivo, Nature Photonics 7(12) (2013) 987-994.

[50] N.P. Cowieson, C.J.C. Edwards-Gayle, K. Inoue, N.S. Khunti, J. Doutch, E. Williams, S. Daniels, G. Preece, N.A. Krumpa, J.P. Sutter, M.D. Tully, N.J. Terrill, R.P. Rambo, Beamline B21: high-throughput small-angle X-ray scattering at Diamond Light Source, Journal of Synchrotron Radiation 27(5) (2020) 1438-1446.

[51] C.J.C. Edwards-Gayle, N. Khunti, I.W. Hamley, K. Inoue, N. Cowieson, R. Rambo, Design of a multipurpose sample cell holder for the Diamond Light Source high-throughput SAXS beamline B21, Journal of Synchrotron Radiation 28(1) (2021) 318-321.

[52] P. Malo de Molina, S. Lad, M.E. Helgeson, Heterogeneity and its Influence on the Properties of Difunctional Poly(ethylene glycol) Hydrogels: Structure and Mechanics, Macromolecules 48(15) (2015) 5402-5411.

[53] N. Pandit, T. Trygstad, S. Croy, M. Bohorquez, C. Koch, Effect of Salts on the Micellization, Clouding, and Solubilization Behavior of Pluronic F127 Solutions, Journal of Colloid and Interface Science 222(2) (2000) 213-220.

[54] S.F. Khattak, S.R. Bhatia, S.C. Roberts, Pluronic F127 as a Cell Encapsulation Material: Utilization of Membrane-Stabilizing Agents, Tissue Engineering 11(5-6) (2005) 974-983.

[55] M. Au - Müller, J. Au - Becher, M. Au - Schnabelrauch, M. Au - Zenobi-Wong, Printing Thermoresponsive Reverse Molds for the Creation of Patterned Two-component Hydrogels for 3D Cell Culture, JoVE (77) (2013) e50632.

[56] E. Gioffredi, M. Boffito, S. Calzone, S.M. Giannitelli, A. Rainer, M. Trombetta, P. Mozetic, V. Chiono, Pluronic F127 Hydrogel Characterization and Biofabrication in Cellularized Constructs for Tissue Engineering Applications, Procedia CIRP 49 (2016) 125-132.

[57] V.A. Feitosa, V.C.d. Almeida, B. Malheiros, R.D.d. Castro, L.R.S. Barbosa, N.N.P. Cerize, C.d.O. Rangel-Yagui, Polymeric micelles of pluronic F127 reduce hemolytic potential of amphiphilic drugs, Colloids and Surfaces B: Biointerfaces 180 (2019) 177-185.

[58] Z. Zhao, X. Kuang, C. Yuan, H.J. Qi, D. Fang, Hydrophilic/Hydrophobic Composite Shape-Shifting Structures, ACS Applied Materials & Interfaces 10(23) (2018) 19932-19939.

[59] D.J. Waters, K. Engberg, R. Parke-Houben, L. Hartmann, C.N. Ta, M.F. Toney, C.W. Frank, Morphology of Photopolymerized End-Linked Poly(ethylene glycol) Hydrogels by Small-Angle X-ray Scattering, Macromolecules 43(16) (2010) 6861-6870.

[60] R.K. Prud'homme, G. Wu, D.K. Schneider, Structure and Rheology Studies of Poly(oxyethylene−oxypropylene−oxyethylene) Aqueous Solution, Langmuir 12(20) (1996) 4651-4659.

[61] J.S. Higgins, H.C. Benoit, Polymer and neutron scattering, Clarendon Press, Oxford, 1994.

[62] C.J.C. Edwards-Gayle, J.K. Wychowaniec, Characterization of Peptide-Based Nanomaterials, in: M.A. Elsawy (Ed.), Peptide Bionanomaterials: From Design to Application, Springer International Publishing, Cham, 2023, pp. 255-308.

[63] P. Alexandridis, B. Lindman, Amphiphilic block copolymers: self-assembly and applications, Elsevier2000.